**Supporting information**

# Surface anions-mediated dynamic interfacial free water enriched microenvironment on $RuO_2$ for efficient acidic oxygen evolution

Liqing Wu [a,b,1], Wenxia Huang [a,1], Bingbing Zhao [a], Ping Cai [a,*], Wei Luo [a,*]

[a] *College of Chemistry and Molecular Sciences, Wuhan University, Wuhan 430072, Hubei, China*
[b] *School of Physics and Optoelectronic Engineering, Hainan University, Haikou 570228, Hainan, China*
* Corresponding author. E-mail: applecaiping@163.com (P. Cai), wluo@whu.edu.cn (W. Luo).
1 Contributed equally to this work.

## Experimental Section

### Chemicals and Material Synthesis

### Chemicals.

All reagents are of analytical grade and used without purification. Ruthenium acetylacetonate ($Ru(acac)_3$, Changcheng Chemical, 98%), trioctylphosphine oxide (TOPO, Aladdin Industrial, 98%), ruthenium chloride ($RuCl_3$, Changcheng Chemical, 98.0%), oleic acid (OA, Aladdin Industrial, AR), dodecylamine (DDA, Aladdin Industrial, 98%), hexane (Kelong Chemical, AR), absolute ethanol (Sinopharm Chemical Reagent, 99.7%), sulfuric acid ($H_2SO_4$, Sinopharm Chemical Reagent, 95.0 ~ 98.0%), isopropanol (Sinopharm Chemical Reagent, 99.7%), Nafion® 117 solution (Sigma-Aldrich, ~ 5% in a mixture of lower aliphatic alcohols and water), and commercial $RuO_2$ (Changcheng Chemical, 99%).

### Synthesis of $RuP_{0.4}O_x$.

In a typical synthesis, 40 mg $Ru(acac)_3$ and 1 g TOPO were added into a 100 mL two-neck round-bottomed flask. The mixture was heated to 120 °C under vigorous magnetic stirring and maintained for 10 min under vacuum to eliminate residual low-boiling solvents and oxygen. Following nitrogen purging, the system was gradually heated to 320 °C at a controlled rate of 10 °C $min^{-1}$ and held for 1 h. The

resulting black suspension was cooled down to room temperature, then washed with ethanol and hexane via centrifugation for several times. Finally, the collected precursor was vacuum-dried, then uniformly loaded onto certain amount of XC-72R carbon black, and annealed at 400 °C for 1 h in air to obtain $RuP_{0.4}O_x$.

**Synthesis of pristine $RuO_2$.**

The synthesis of $RuO_2$ nanoparticles followed a procedure similar to previous reports with minor modifications [1]. Typically, 103.7 mg of $RuCl_3$, 0.5 mL OA and 3 mL DDA were prepared in a two-neck flask. The mixture was vigorously magnetically stirred and heated to 120 °C for 10 min. After purging with nitrogen, the system was gradually heated to 320 °C with a speed of 10 °C $min^{-1}$ and kept for 1 h. The washing and loading procedures for $RuO_2$ were identical to those employed in the synthesis of $RuP_{0.4}O_x$. Finally, the collected precursor was annealed at 500 °C for 1 h in air to obtain $RuO_2$.

**Materials characterization.**

The X-ray powder diffraction (XRD) patterns were obtained on a Rigaku Miniflex600 X-ray powder diffractometer equipped with a Cu $K_\alpha$ radiation source (λ = 0.154178 nm). All of the diffraction data were collected in a $2\theta$ range from 10° to 80° at a scanning rate of 10° $min^{-1}$. The transmission electron microscopy (TEM) images were performed with JEM-2100 Plus operated at 200 kV. High-angle annular dark-field scanning transmission electron microscopy (HAADF-STEM) was conducted by JEM-ARM200CF. Scanning transmission electron microscopy (STEM) imaging and energy-dispersive X-ray spectroscopy (EDX) mapping were acquired on a JEOL JEM-ARM200CF microscope operated at 200 kV with a Schottky cold-field emission gun in Wuhan University. The EDX elemental mapping was carried using the JEOL SDD-detector with two 100 $mm^2$ X-ray sensor. Inductively coupled plasma atomic emission spectroscopy (ICP-AES) was conducted on the Agilent 5110. X-ray photoelectron spectroscopy (XPS) measurement was carried out with a Thermo Fischer ESCALAB 250Xi spectrophotometer.

*Operando* attenuated total reflectance surface-enhanced infrared absorption spectroscopy (ATR-SEIRAS) was carried out with Bruker Invenio R, equipped with a liquid nitrogen-cooled detector. A homemade IR cell with a polished Si prism was employed as experimental apparatus.

**Electrochemical characterizations**

All electrochemical experiments were performed at room temperature using a CHI 760E electrochemical workstation with a standard three-electrode system. The electrocatalyst decorated rotating disk electrode with glassy carbon was used as the working electrode. The diameter of glassy carbon was 5 mm and the disk area was 0.19625 $cm^2$. The carbon rod and $Hg/Hg_2Cl_2$ electrode (saturated KCl solution) were applied as the counter electrode and reference electrode, respectively. The reference electrode potential was transformed to the reversible hydrogen electrode potential by a formula: $E$ (V vs. RHE) = $E$ (V vs. $Hg/Hg_2Cl_2$) + 0.059 × pH (V) + 0.25 (V). The electrocatalyst was prepared with a recipe of 5 mg pre-synthesized catalyst and 1.0 mL solvent of isopropyl alcohol containing 0.1 wt.% Nafion, which was sonicated for 2 h to be a homogeneous catalyst ink. Then 18 μL catalyst ink was dripped on the surface of the glassy carbon with the total loading of 0.09 mg. As comparison, the same amount of commercial $RuO_2$ catalyst inks was also prepared in same method. Linear sweep voltammetry (LSV) was conducted in 0.5 M $H_2SO_4$ with a scan rate of 5 mV $s^{-1}$ in $O_2$ saturated atmosphere with the potential range from 1.0 V to 1.5 V (vs. $Hg/Hg_2Cl_2$). Cyclic voltammetry (CV) measurements were recorded in the non-Faradaic region with different scan rates (10, 20, 30, 40, and 50 mV $s^{-1}$). The electrochemically active surface areas (ECSA) were estimated from the electrochemical double-layer capacitance ($C_{dl}$) of the catalytic surface. The $C_{dl}$ was determined by plotting the $\Delta j$ / 2 ($\Delta j = j^a - j^c$, where $j^a$ is the anodic current and $j^c$ is the cathodic current at the middle voltage) against the scan rate, where the slope is equal to $C_{dl}$. The ECSA values were obtained from the electrochemical double-layer capacitance of the catalytic surface, according to: ECSA = $C_{dl}$ / $C_s$, Where $C_s$ is the specific capacitance of the sample (set as 0.035 mF $cm^{-2}$). Electrochemical impedance

spectroscopy (EIS) measurements were carried out with the AC impedance spectra from 2.158 × $10^5$ kHz to 0.01 kHz and a voltage perturbation of 5 mV. The real part of the resistance at 1 kHz was taken as the uncompensated resistance ($R_u$) and was used to obtain the *i*R-free potential ($E_{iR\text{-free}}$) according to the following equation, $E_{iR\text{-free}} = E - iR_u$, where $E$ is the measured potential and $i$ is the corresponding current. Chronopotentiometric measurements were performed on a constant current of 10 mA $cm^{-2}$. The following mentioned potentials are standard hydrogen electrode potential scales unless specified. In order to better reflect the performance and close to the actual application situation, we have adopted the current density recorded at a high potential of 1.53 V vs. RHE to calculate the mass activity. The mass activity is calculated by a formula: $j^m = (j \times A) / m$, where $j^m$ is the mass activity, $j$ is the current density normalized by the geometric area, A is the electrode area, and m is the Ru loading mass of electrocatalyst on electrode.

To evaluate the kinetic isotope effect (KIE), LSV measurements was performed in both protonic (0.5 M $H_2SO_4$ in $H_2O$) and deuteric (0.5 M $D_2SO_4$ in $D_2O$) electrolytes. The reference electrode potential was transformed to the reversible hydrogen electrode potential by a formula:

$$E\ (V\ vs.\ RDE) = E\ (V\ vs.\ Hg/Hg_2Cl_2) + 0.059 \times pD\ (V) + 0.25\ (V) + 0.013$$

where the pD value of the deuterated solution was obtained by adding 0.41 to the pH reading measured with a glass membrane electrode connected to a pH meter, which introduces a potential shift of 0.059 × 0.41 (V). The correction term of 0.013 accounts for the difference in the standard equilibrium potentials between the deuterium ($D_2/D^+$) and proton ($H_2/H^+$) couples.

The overpotentials of the OER in the protonic and deuteric electrolytes were determined using equations:

$$\eta = E\ (V\ vs.\ RHE) - 1.229\ V$$

$$\eta = E\ (V\ vs.\ RDE) - 1.262\ V$$

the KIE was then evaluated as:

$$\mathrm{KIE} = \left|\frac{j_{H_2O}}{j_{D_2O}}\right|_{\eta}$$

where $j_{H_2O}$ and $j_{D_2O}$ are the catalytic current density at the same overpotential η in the protonic and deuteric electrolytes, respectively.

**DFT calculations**

All the theoretical calculations were conducted by using CASTEP code of the Materials Studio package of Accelrys Inc with generalized gradient approximation method (GGA) and the Perdew-Burke-Ernzerh (PBE) functional to describe the exchange and correlation interactions. The interaction between valence electrons and ionic cores was described by Ultrasoft pseudopotential. The cutoff energy was set as 400 eV and the self-consistent field (SCF) tolerance was $1 \times 10^{-6}$ eV. Given the experimental results and the fact that $RuO_2$ (110) is the most thermodynamically stable lattice plane, we choose (110) surface as the model of $RuP_{0.4}O_x$ and $RuO_2$ for calculation. The smearing method of Methfessel-Paxton (MP) and smearing widths of 0.1 eV were applied to optimize the geometric. The Brillouin zone was sampled using the Monkhorst Pack method, and the number of k points was set according to the model, of which 4 × 4 × 1 was set for all the geometric optimization. The thickness of vacuum layer along the z-direction is set as 15 Å to separate the upper and lower surfaces. For all calculations, the atoms in the bottom layer were fixed in the equilibrium positions, while the rest of the atoms were fully relaxed. The adsorption free energies of various intermediates on a certain surface are calculated by ΔG = ΔE + ΔZPE − TΔS, where ΔE is the DFT based adsorption energy of intermediate, ΔZPE and TΔS are the correction of zero point energy and entropy, respectively.

In the traditional AEM pathway, the Gibbs free energy changes for the OER were calculated using the following Equations:

$H_2O + M^* \rightarrow M\text{-}OH^* + H^+ + e^-$

$M\text{-}OH^* \rightarrow M\text{-}O^* + H^+ + e^-$

$H_2O + M\text{-}O^* \rightarrow M\text{-}OOH^* + H^+ + e^-$

$M\text{-}OOH^* \rightarrow M\text{-}OO^* + H^+ + e^-$ ($M\text{-}OO^* \rightarrow M^* + O_2$)

where * denotes adsorption active site on the substrate.

For the proposed $PO_x$-AEM pathway, the Gibbs free energy changes for the OER were calculated using the following Equations:

$H_2O + PO_x\text{-}M^* \rightarrow H^*\text{-}PO_x\text{-}M\text{-}OH^*$

$H^*\text{-}PO_x\text{-}M\text{-}OH^* \rightarrow PO_x\text{-}M\text{-}OH^* + H^+ + e^-$

$PO_x\text{-}M\text{-}OH^* \rightarrow H^*\text{-}PO_x\text{-}M\text{-}O^*$

$H^*\text{-}PO_x\text{-}M\text{-}O^* \rightarrow PO_x\text{-}M\text{-}O^* + H^+ + e^-$

$H_2O + PO_x\text{-}M\text{-}O^* \rightarrow H^*\text{-}PO_x\text{-}M\text{-}OOH^*$

$H^*\text{-}PO_x\text{-}M\text{-}OOH^* \rightarrow PO_x\text{-}M\text{-}OOH^* + H^+ + e^-$

$PO_x\text{-}M\text{-}OOH^* \rightarrow H^*\text{-}PO_x\text{-}M\text{-}OO^*$ ($H^*\text{-}PO_x\text{-}M\text{-}OO^* \rightarrow PO_x\text{-}M^* + O_2 + H^+ + e^-$)

where * denotes adsorption active site on the substrate.

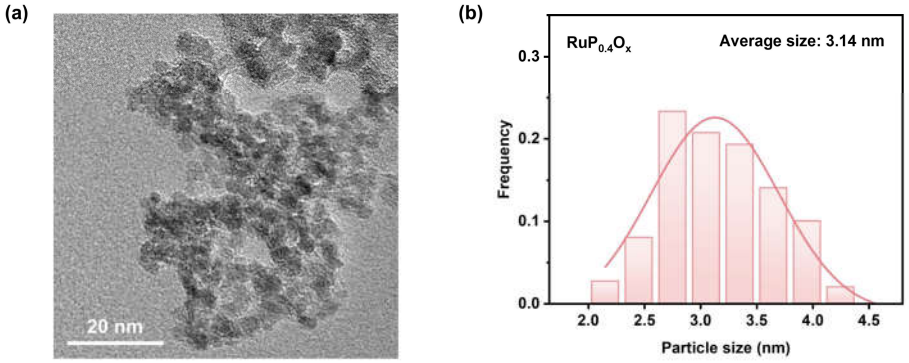


**Figure S1.** TEM image (a) and the corresponding particle size distribution (b) of $RuP_{0.4}O_x$, derived by counting more than 150 nanoparticles.

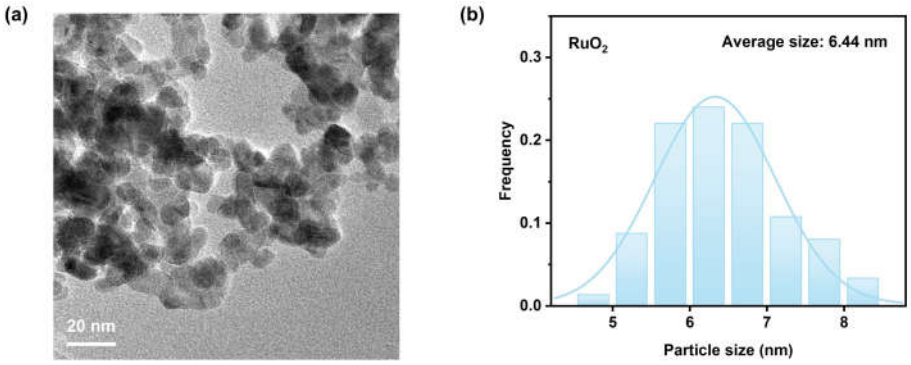


**Figure S2.** TEM image (a) and the corresponding particle size distribution (b) of $RuO_2$, derived by counting more than 150 nanoparticles.

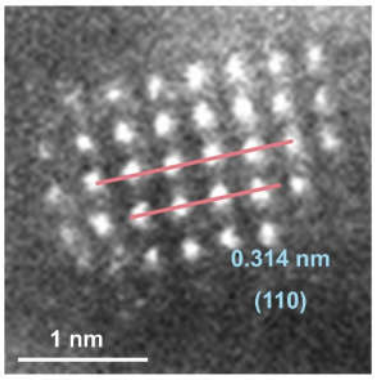


**Figure S3.** The high resolution HAADF-STEM image of $RuP_{0.4}O_x$.

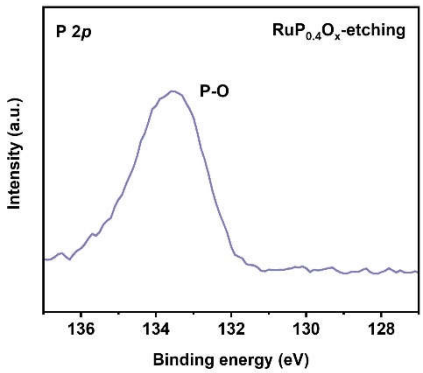


**Figure S4.** High resolution XPS spectrum of P 2*p* for $RuP_{0.4}O_x$ catalyst after the surface etching.

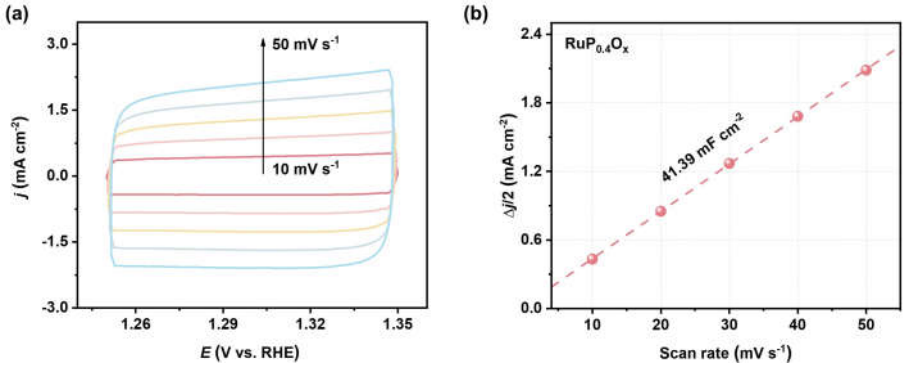


**Figure S5.** CV curves recorded under different sweep rates (a) and the corresponding calculated electrochemical $C_{dl}$ value (b) of $RuP_{0.4}O_x$.

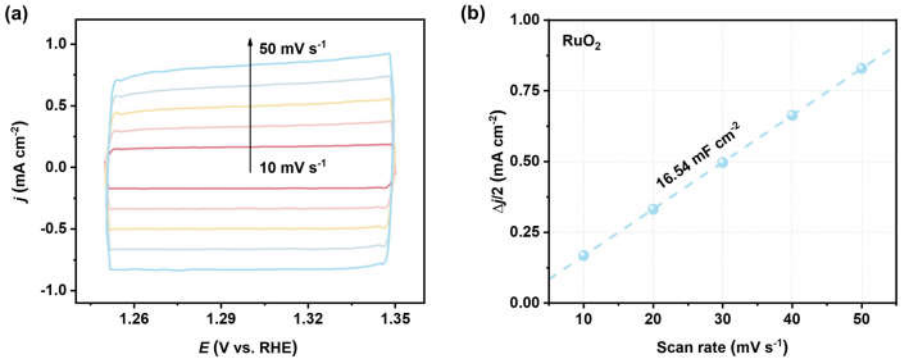


**Figure S6.** CV curves recorded under different sweep rates (a) and the corresponding calculated electrochemical $C_{dl}$ value (b) of $RuO_2$.

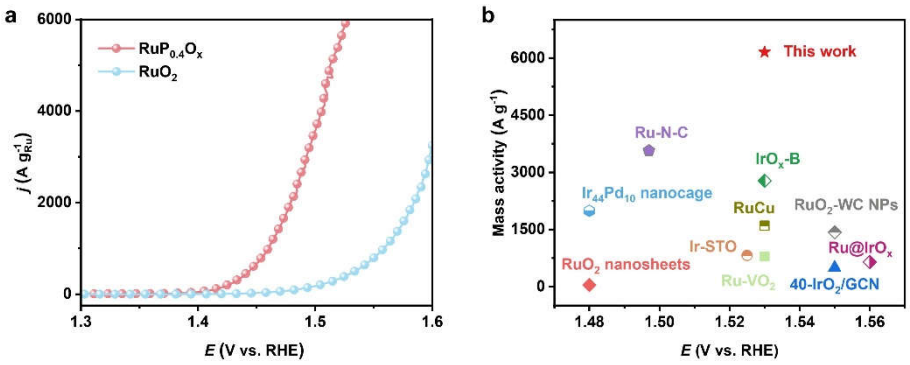


**Figure S7.** (a) The LSV curves were normalized with the mass of Ru for $RuP_{0.4}O_x$ and $RuO_2$ catalysts. (b) Comparison of the mass activities between $RuP_{0.4}O_x$ and other recently reported catalysts.

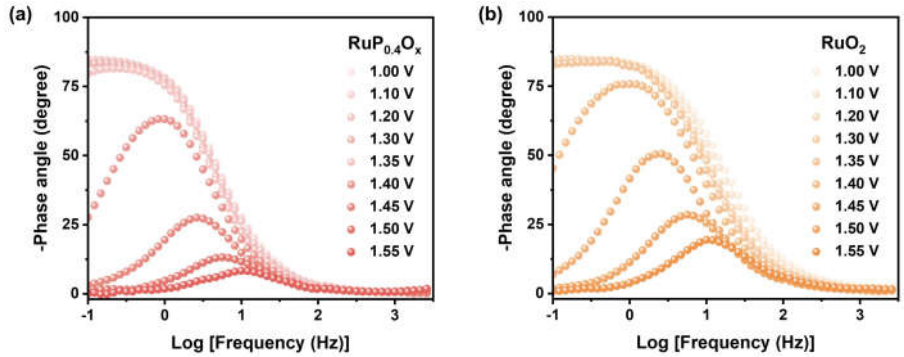


**Figure S8.** Bode phase plots of $RuP_{0.4}O_x$ (a) and $RuO_2$ (b) at different potentials.

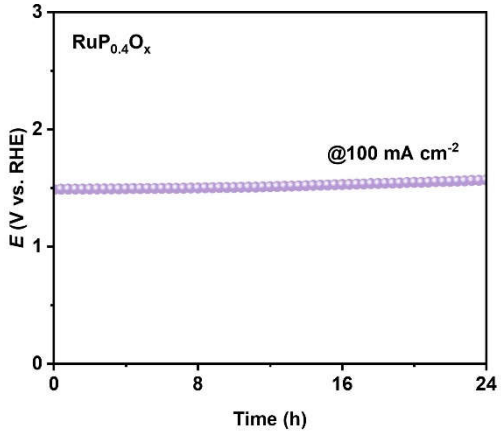


**Figure S9.** Stability test of $RuP_{0.4}O_x$ at the current density of 100 mA $cm^{-2}$.

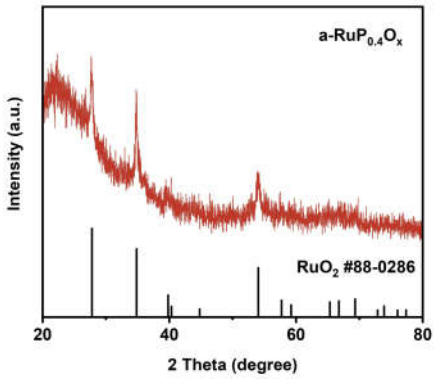


**Figure S10.** XRD pattern of $RuP_{0.4}O_x$ after the stability test (a-$RuP_{0.4}O_x$).

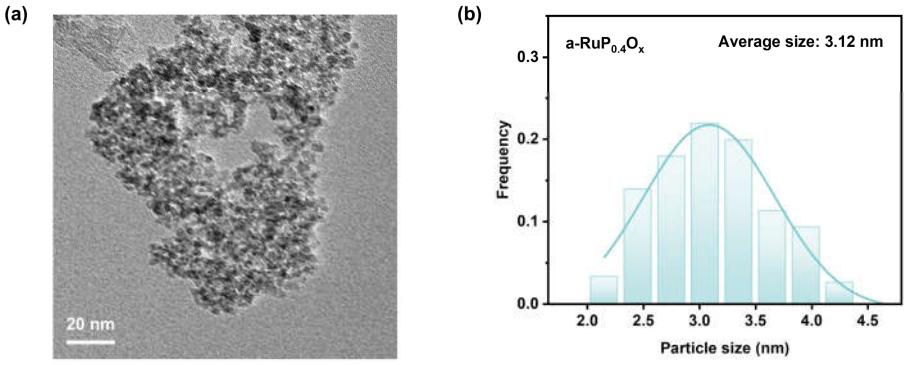


**Figure S11.** TEM image (a) and the corresponding particle size distribution (b) of a-$RuP_{0.4}O_x$, derived by counting more than 150 nanoparticles.

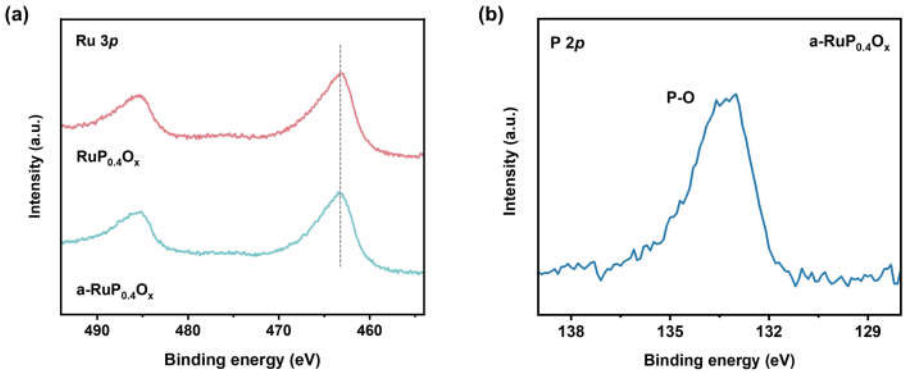


**Figure S12.** (a) High resolution XPS spectra of Ru 3*p* for $RuP_{0.4}O_x$ and a-$RuP_{0.4}O_x$. (b) High resolution XPS spectrum of P 2*p* for a-$RuP_{0.4}O_x$.

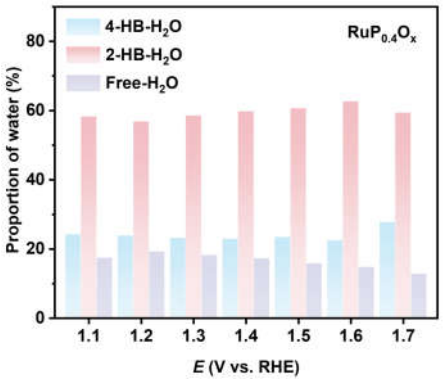


**Figure S13.** The proportions of 4-HB-$H_2O$, 2-HB-$H_2O$, and free-$H_2O$ at varied potentials of $RuP_{0.4}O_x$ catalyst.

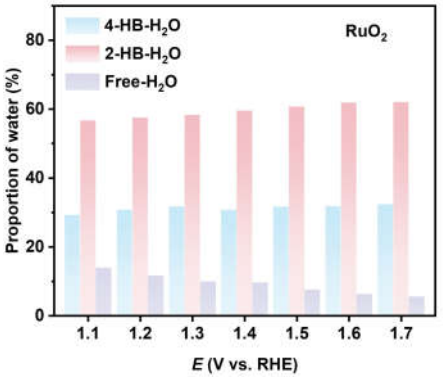


**Figure S14.** The proportions of 4-HB-$H_2O$, 2-HB-$H_2O$, and free-$H_2O$ at varied potentials of $RuO_2$ catalyst.

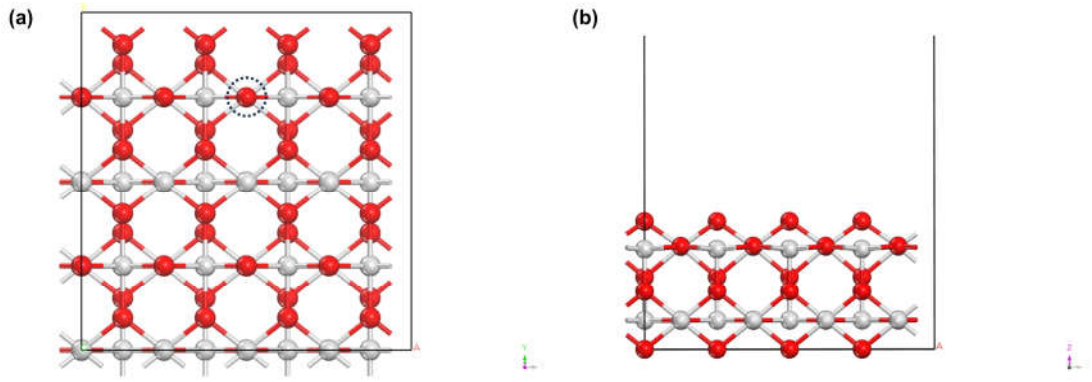


**Figure S15.** The top view (a) and side view (b) of $RuO_2$ (110) surface. The light grey balls and red balls represent Ru atoms and O atoms, respectively. The oxygen atom marked within the black circle corresponds to the bridging oxygen site.

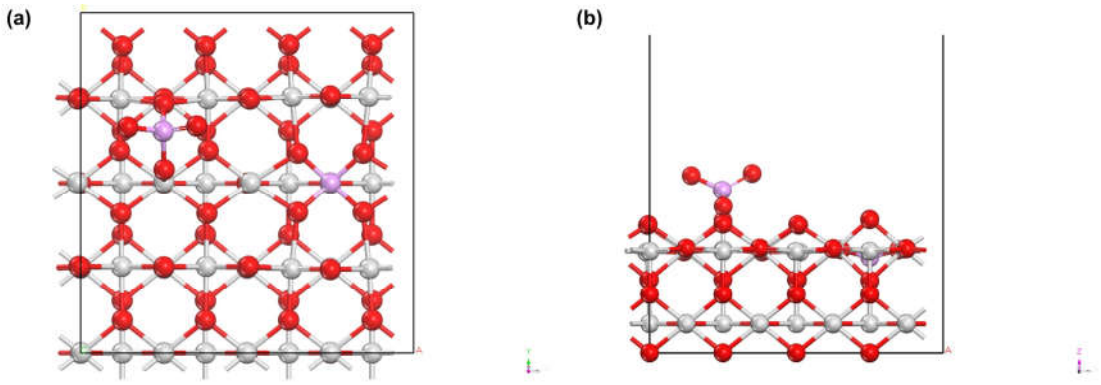


**Figure S16.** The top view (a) and side view (b) of $RuP_{0.4}O_x$ (110) surface. The light grey balls, purple balls, and red balls represent Ru atoms, P atoms, and O atoms, respectively.

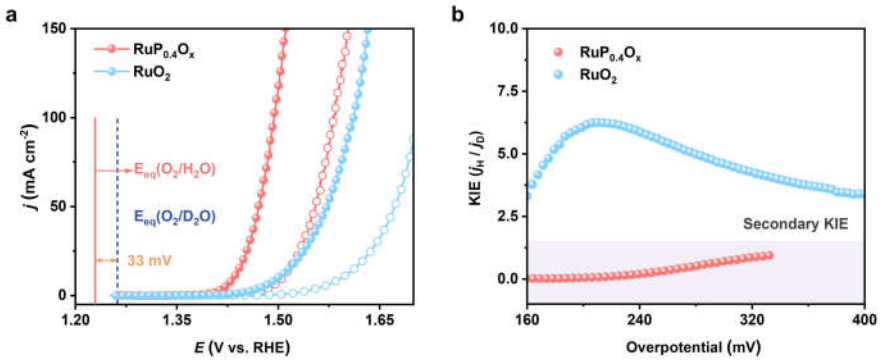


**Figure S17.** (a) LSV curves of $RuP_{0.4}O_x$ and $RuO_2$ recorded in 0.5 M $H_2SO_4$ electrolyte and in 0.5 M $D_2SO_4$ electrolyte, respectively. (b) The KIE curves of $RuP_{0.4}O_x$ and $RuO_2$ derived from (a).

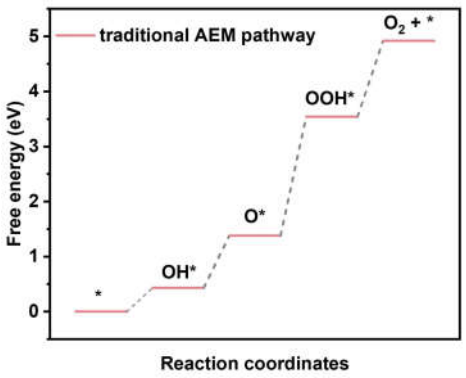


**Figure S18.** The free energy diagram of $RuP_{0.4}O_x$ in traditional AEM pathway. The energy barrier of the potential determining step is 2.16 eV.

**Table S1.** ICP-AES results of all the samples in this work.

| | Ru (wt%) | P (wt%) |
|---|---|---|
| $RuP_{0.4}O_x$ | 8.65 | 1.05 |
| $RuO_2$ | 8.40 | ~ |

**Table S2.** Comparison of the mass activity employed in this study with other electrocatalysts.

| Catalyst | Electrolyte | Mass activity | Reference |
|---|---|---|---|
| $RuP_{0.4}O_x$ | 0.5 M $H_2SO_4$ | 6155 A $g_{Ru}^{-1}$@1.53 $V_{RHE}$ | This work |
| $Ir_{44}Pd_{10}$ nanocage | 0.1 M $HClO_4$ | 1990 A $g_{Ir}^{-1}$@1.48 $V_{RHE}$ | 2 |
| Ru-$VO_2$ | 0.5 M $H_2SO_4$ | 788.87 A $g_{metal}^{-1}$@1.53 $V_{RHE}$ | 3 |
| Ir-STO | 0.1 M $HClO_4$ | 820 A $g_{Ir}^{-1}$@1.525 $V_{RHE}$ | 4 |
| $RuO_2$ nanosheets | 0.1 M $HClO_4$ | 42 A $g_{Ru}^{-1}$@1.48 $V_{RHE}$ | 5 |
| Ru-N-C | 0.5 M $H_2SO_4$ | 3571 A $g_{metal}^{-1}$@1.497 $V_{RHE}$ | 6 |
| RuCu | 0.5 M $H_2SO_4$ | 1600 A $g_{Ru}^{-1}$@1.53 $V_{RHE}$ | 7 |
| 40-$IrO_2$/GCN | 0.5 M $H_2SO_4$ | 497 A $g_{Ir}^{-1}$@1.55 $V_{RHE}$ | 8 |
| Ru@$IrO_x$ | 0.05 M $H_2SO_4$ | 644.8 A $g_{oxide}^{-1}$@1.56 $V_{RHE}$ | 9 |
| $IrO_x$-B | 0.1 M $HClO_4$ | 2779 A $g_{Ir}^{-1}$@1.53 $V_{RHE}$ | 10 |
| $RuO_2$-WC NPs | 0.5 M $H_2SO_4$ | 1430 A $g_{Ru}^{-1}$@1.55 $V_{RHE}$ | 11 |

**Table S3.** Comparison of overpotentials (at the current density of 10 $mAcm^{-2}$) and stabilities employed in this study with other electrocatalysts.

| Catalyst | Electrolyte | $\eta_{10}$ / mV | Stability | Reference |
|---|---|---|---|---|
| $RuP_{0.4}O_x$ | 0.5 M $H_2SO_4$ | 200 | 500 h @ 10 mA $cm^{-2}$ | This work |
| Co-Ru@$RuO_2$ 9:1 | 0.5 M $H_2SO_4$ | 203 | 420 h @ 10 mA $cm^{-2}$ | 12 |
| $Nd_{0.1}RuO_x$/CC | 0.5 M $H_2SO_4$ | 211 | 50 h @ 10 mA $cm^{-2}$ | 13 |
| Ni-$RuO_2$ | 0.1 M $HClO_4$ | 214 | 205 h @ 10 mA $cm^{-2}$ | 14 |
| a-$RuO_x$-l | 0.5 M $H_2SO_4$ | 215 | 300 h @ 10 mA $cm^{-2}$ | 15 |
| Ga-$RuO_2$ | 0.5 M $H_2SO_4$ | 217.5 | 150 h @ 10 mA $cm^{-2}$ | 16 |

| | | | | |
|---|---|---|---|---|
| $RuNi_2$@G-250 | 0.5 M $H_2SO_4$ | 227 | 24 h @ 10 mA $cm^{-2}$ | 17 |
| SS Pt-$RuO_2$ HNSs | 0.5 M $H_2SO_4$ | 228 | 100 h @ 10 mA $cm^{-2}$ | 18 |
| Ru-$VO_2$ | 0.5 M $H_2SO_4$ | 228 | 60 h @ 10 mA $cm^{-2}$ | 3 |
| $S_H$-RuCuO NRs/C | 0.5 M $H_2SO_4$ | 231 | 250 h @ 10 mA $cm^{-2}$ | 19 |
| $RuO_2$ nanosheets | 0.1 M $HClO_4$ | 255 | 6 h @ 10 mA $cm^{-2}$ | 5 |
| Ru-N-C | 0.5 M $H_2SO_4$ | 267 | 30 h @ 1.5 V (vs.RHE) | 6 |
| $Y_2MnRuO_7$ | 0.1 M $HClO_4$ | 270 | 45 h @ 10 mA $cm^{-2}$ | 20 |

## Reference


[1] S. Liu, Q. Liu, Y. Lv, B. Chen, Q. Zhou, L. Wang, Q. Zheng, C. Che, C. Chen, *Chem. Commun.*, **2017**, 53, 13153–13156.

[2] J. Zhu, Z. Chen, M. Xie, Z. Lyu, M. Chi, M. Mavrikakis, W. Jin, Y. Xia, *Angew. Chem. Int. Ed.*, **2019**, 58, 7244–7248.

[3] Z. Niu, Z. Lu, Z. Qiao, S. Wang, X. Cao, X. Chen, J. Yun, L. Zheng, D. Cao, *Adv. Mater.*, **2023**, 36, 2310690.

[4] X. Liang, L. Shi, Y. Liu, H. Chen, R. Si, W. Yan, Q. Zhang, G. D. Li, L. Yang, X. Zou, *Angew. Chem. Int. Ed.*, **2019**, 58, 7631–7635.

[5] S. Laha, Y. Lee, F. Podjaski, D. Weber, V. Duppel, L. M. Schoop, F. Pielnhofer, C. Scheurer, K. Müller, U. Starke, K. Reuter, B. V. Lotsch, *Adv. Energy Mater.*, **2019**, 9, 1803795.

[6] L. Cao, Q. Luo, J. Chen, L. Wang, Y. Lin, H. Wang, X. Liu, X. Shen, W. Zhang, W. Liu, Z. Qi, Z. Jiang, J. Yang, T. Yao, *Nat. Commun.*, **2019**, 10, 4849.

[7] Y. Li, W. Zhou, X. Zhao, W. Cheng, H. Su, H. Zhang, M. Liu, Q. Liu, *ACS Appl. Energy Mater.*, **2019**, 2, 7483–7489.

[8] J. Chen, P. Cui, G. Zhao, K. Rui, M. Lao, Y. Chen, X. Zheng, Y. Jiang, H. Pan, S. X. Dou, W. Sun, *Angew. Chem. Int. Ed.*, **2019**, 58, 12540–12544.

[9] J. Shan, C. Guo, Y. Zhu, S. Chen, L. Song, M. Jaroniec, Y. Zheng, S.-Z. Qiao, *Chem*, **2019**, 5, 445–459.

[10] Z. Cheng, Y. Pi, Q. Shao, X. Huang, *Science China Materials*, **2021**, 64,

2958–2966.

[11] S. C. Sun, H. Jiang, Z. Y. Chen, Q. Chen, M. Y. Ma, L. Zhen, B. Song, C. Y. Xu, *Angew. Chem. Int. Ed.*, **2022**, 61, e202202519.

[12] J. Chen, Y. Ma, C. Cheng, T. Huang, R. Luo, J. Xu, X. Wang, T. Jiang, H. Liu, S. Liu, T. Huang, L. Zhang, W. Chen, *J. Am. Chem. Soc.*, **2025**, 147, 8720–8731.

[13] L. Li, G. Zhang, J. Xu, H. He, B. Wang, Z. Yang, S. Yang, *Adv. Funct. Mater.*, **2023**, 33, 2213304.

[14] Z.-Y. Wu, F.-Y. Chen, B. Li, S.-W. Yu, Y. Z. Finfrock, D. M. Meira, Q.-Q. Yan, P. Zhu, M.-X. Chen, T.-W. Song, Z. Yin, H.-W. Liang, S. Zhang, G. Wang, H. Wang, *Nat. Mater.*, **2023**, 22, 100–108.

[15] Y. Mu, J. Fan, T. Gao, L. Wang, L. Zhang, X. Zou, W. Zheng, Y. W. Zhang, Z. G. Yu, X. Cui, *Angew. Chem. Int. Ed.*, **2025**, 64, e202504876.

[16] L. Wu, W. Huang, D. Li, H. Jia, B. Zhao, J. Zhu, H. Zhou, W. Luo, *Angew. Chem. Int. Ed.*, **2024**, 64, e202413334.

[17] X. Cui, P. Ren, C. Ma, J. Zhao, R. Chen, S. Chen, N. P. Rajan, H. Li, L. Yu, Z. Tian, D. Deng, *Adv. Mater.*, **2020**, 32, 1908126.

[18] J. Wang, H. Yang, F. Li, L. Li, J. Wu, S. Liu, T. Cheng, Y. Xu, Q. Shao, X. Huang, *Sci. Adv.*, **2022**, 8, eabl9271.

[19] Q. Yao, Z. Yu, Y.-H. Chu, Y.-H. Lai, T.-S. Chan, Y. Xu, Q. Shao, X. Huang, *Nano Res.*, **2022**, 15, 3964–3970.

[20] D. Galyamin, J. Torrero, I. Rodríguez, M. J. Kolb, P. Ferrer, L. Pascual, M. A. Salam, D. Gianolio, V. Celorrio, M. Mokhtar, D. Garcia Sanchez, A. S. Gago, K. A. Friedrich, M. A. Peña, J. A. Alonso, F. Calle-Vallejo, M. Retuerto, S. Rojas, *Nat. Commun.*, **2023**, 14, 2010.